Supporting Information: Increased thermal conductivity and decreased electron-phonon coupling factor of the aluminum-scandium intermetallic phase (Al_3Sc) compared to solid solutions

Daniel Hirt[1], Md. Rafiqul Islam[1], Md. Shafkat Bin Hoque[1], William Hutchins[1], Sara Makarem[2], Megan K. Lenox[2], William T. Riffe[2], Jon F. Ihlefeld[2,3], Ethan A. Scott[1], Giovanni Esteves[4], Patrick E. Hopkins[1,2,5]

[1.] Department of Mechanical and Aerospace Engineering, University of Virginia, Charlottesville, VA 22904, USA

[2.] Department of Materials Science and Engineering, University of Virginia, Charlottesville, VA 22904, USA

[3.] Charles L. Brown Department of Electrical and Computer Engineering, University of Virginia, Charlottesville, Virginia 22904, USA

[4.] Microsystems Engineering, Science and Applications (MESA), Sandia National Laboratories, Albuquerque, NM 87123, USA

[5.] Department of Physics, University of Virginia, Charlottesville, VA 22904, USA

a) **Author to whom correspondence should be addressed:** pehopkins@virginia.edu

S1. TDTR FITTING

To increase the sensitivity of our TDTR measurement to the in-plane thermal conductivity of the AlSc films, we use a 1.2 MHz pump modulation frequency in conjunction with a 20x objective to provide a relatively small spot size with a $1/e^2$ effective diameter of 4.4 μm. We use a three-layer heat diffusion model to determine the in-plane thermal conductivity of aluminum scandium fitting for both the in-plane and cross-plane thermal conductivity of aluminum scandium for the 25 °C 150 °C, and 300 °C films, and solely fitting for in-plane thermal conductivity for the 450 °C and 25 °C annealed films.[1,2] Because the 450 °C and 25 °C annealed films have significantly higher thermal conductivities we become insensitive to their cross-plane thermal conductivity and thus can fit for only in-plane thermal conductivity. Our fitting results, shown in Table S1, indicate isotropic thermal conductivity within uncertainty, which is expected for randomly oriented polycrystals such as our films, and are shown in Table S1.[3] Fig. S1 exhibits an example best-fit of the thermal model compared to the ratio of the in-phase and out-of-phase data ($-V_{in}/V_{out}$) for the 25 °C annealed film. The parameters for our thermal model are depicted in Table S2.

Table S1. Thermal conductivity results for our aluminum scandium films.

	κ_{in} (W m^{-1} K^{-1})	$\Delta\kappa_{in}$ (W m^{-1} K^{-1})	κ_z (W m^{-1} K^{-1})
25 °C	8	3.8	7.13
150 °C	8.6	4.0	11.2
300 °C	11.0	4.1	13.5
450 °C	34.1	8.6	34.1
25 °C annealed	67.5	14.1	67.5

Table S2. Parameters used in sensitivity analysis and the thermal model to determine the in-plane thermal conductivity of aluminum scandium.

	Thermal conductivity W m^{-1} K^{-1}	**Heat capacity, MJ m^{-3} K^{-1}**	**Thermal boundary conductance MW m^{-2} K^{-1}**
AlSc	-	2.302 (Ref. 4)	-
AlSc/SiO_2	-	-	52.6
SiO_2	1.35 (isotropic)	1.62 (Ref. 5)	-
SiO_2/Si	-	-	230 (Refs. 5,6)
Si	130(isotropic) (Ref. 7)	1.65 (Ref. 6)	-

To determine the thermal boundary conductance of aluminum scandium and SiO_2 as well as the thermal conductivity of SiO_2, we use TDTR with a high modulation frequency (8.4 MHz) and large spot size ($1/e^2$ diameter of 11 μm for the probe and 19 um for the pump) scan of the annealed film. These factors in combination with the annealed film having high cross-plane thermal conductivity results in a TDTR measurement that is sensitive to the thermal conductivity of SiO_2. This measurement also has high sensitivity to the thermal boundary conductance between aluminum scandium and SiO_2, however, because of the nature of our measurement this thermal boundary conductance pathway is a relatively small thermal resistance compared to the other thermal resistances resulting in the measurements for our other films being largely insensitive to it. By using this method, we obtain a value for the thermal conductivity of SiO_2 and the thermal boundary conductance between aluminum scandium and SiO_2 that we then hold constant when fitting for in-plane thermal conductivity across our low modulation frequency measurements. Sensitivities for these measurements are shown in Fig. S2, and details on the methodology used for this sensitivity calculation can be found in previous works[8,9]. The uncertainty in our TDTR

measurements is calculated using Eq. S1 which accounts for spot-to-spot deviations as well as uncertainties in both the assumed thermal properties and fitting procedure.[10]

$$\Delta = \sqrt{(\sigma^2) + (\sum_i \Delta_i^2) + (\sigma_C^2)} \quad \text{(S1)}$$

Where Δ is the total uncertainty, σ is the standard deviation among multiple measurements across different spots, σ_c is the contour uncertainty due to fitting assumptions, and Δ_i is the uncertainty due to an individual parameter. For our in-plane thermal conductivity uncertainty we assume a 10% uncertainty in aluminum scandium heat capacity, SiO_2 thermal conductivity, spot size, and the thermal boundary conductance between aluminum scandium and SiO_2. This range of uncertainty is typical in most TDTR measurements.[10,11] We calculate the uncertainty due to our fitting procedure via the method outlined by Feser *et al*.[12] comparing the residual between our fit and the experimental data for the assumed thermal parameters in our model. For all of our in-plane thermal conductivity measurements, we are highly sensitive to the thermal conductivity of the SiO_2, as indicated in Fig. S2. Thus, by calculating a 2D residual contour of the in-plane thermal conductivity against SiO_2 thermal conductivity, we obtain a direct indication of the uncertainty in our fit due to the assumed SiO_2 thermal conductivity. Examples of these residual plots are shown in Fig. S3 and Fig. S4 for the 150 °C film and 25 °C film respectively. For all of our measurements except for the 25 °C film our fitting procedure had low residuals of less than .01 and for these measurements we used a residual threshold of .025 to bound our fit indicating that any fit with a residual under .025 is acceptable and contributes to our uncertainty.

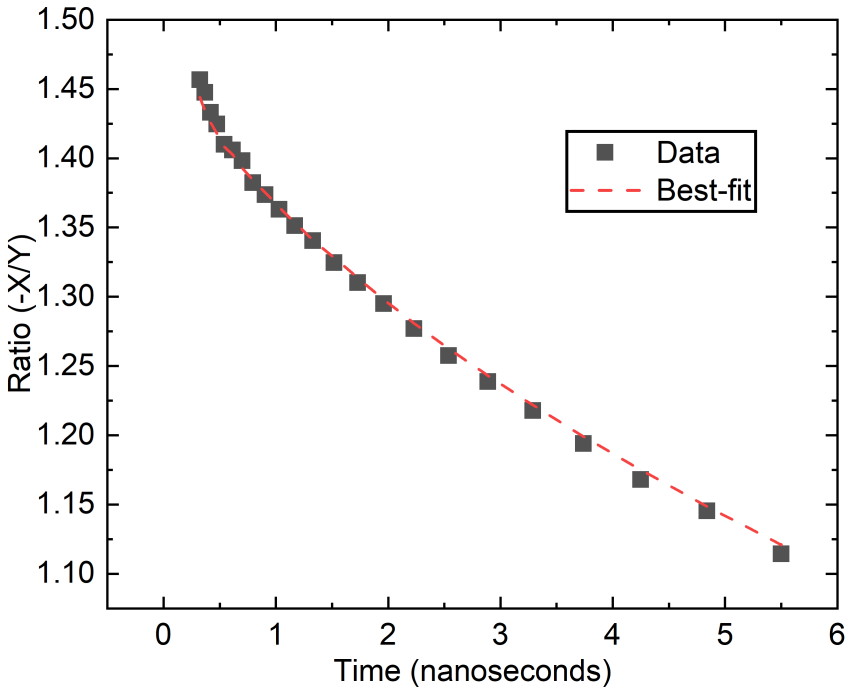

Figure S1. Example fit for the low modulation frequency 450 °C film data. This results in a best fit in-plane thermal conductivity of the film of 34.2 W m^{-1} K^{-1}.

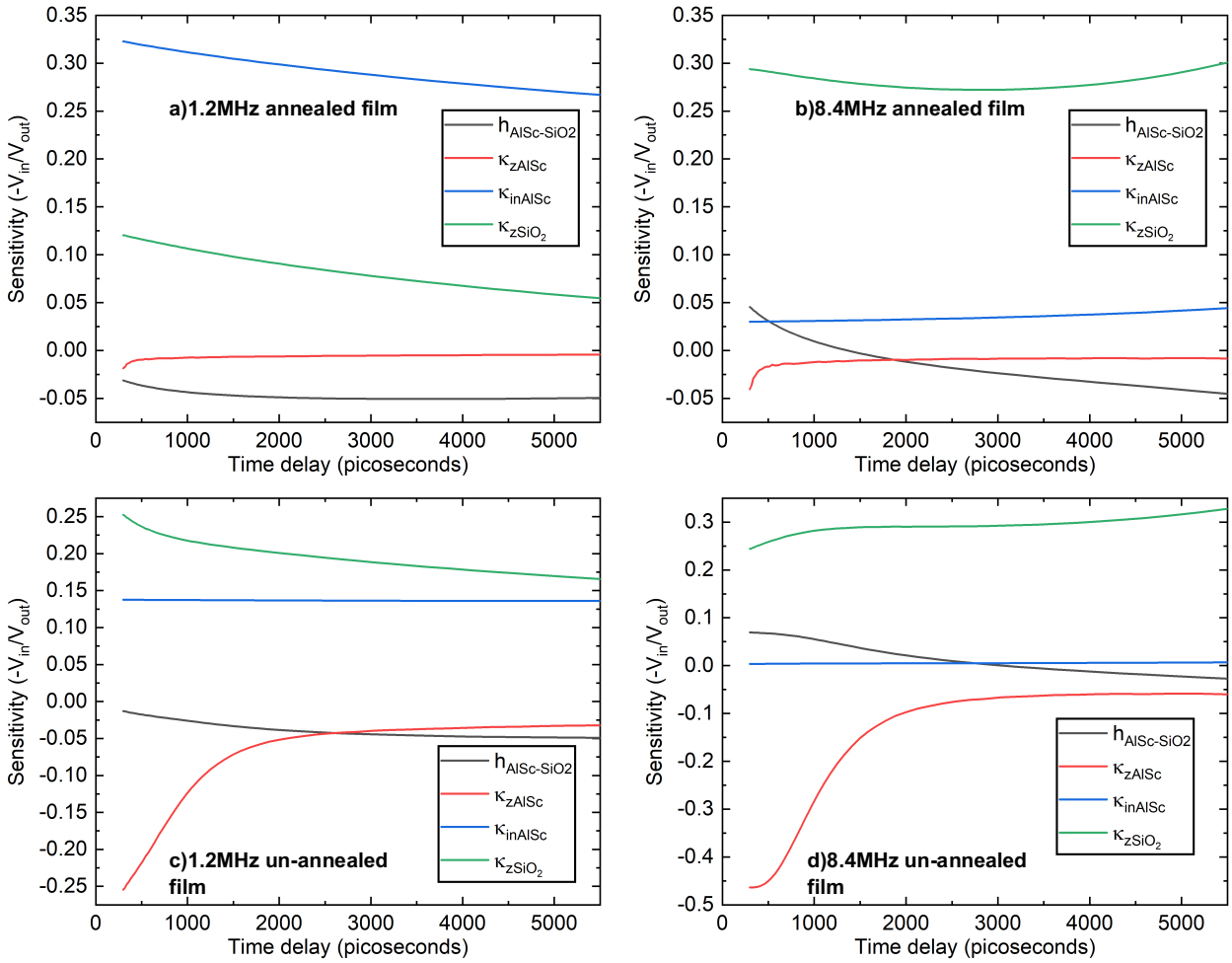

Fig. S2. a) Sensitivity for the 1.2 MHz measurement of the 25 °C annealed film. The cross-plane thermal conductivity, in-plane thermal conductivity, and thermal boundary conductance are denoted by κ_z, κ_{in} and h respectively. **b)** Sensitivity for the 8.4 MHz measurement of the 25 °C annealed film. **c)** Sensitivity for the 1.2 MHz measurement of the 25 °C unannealed film. **d)** Sensitivity for the 8.4 MHz measurement of the 25 °C unannealed film.

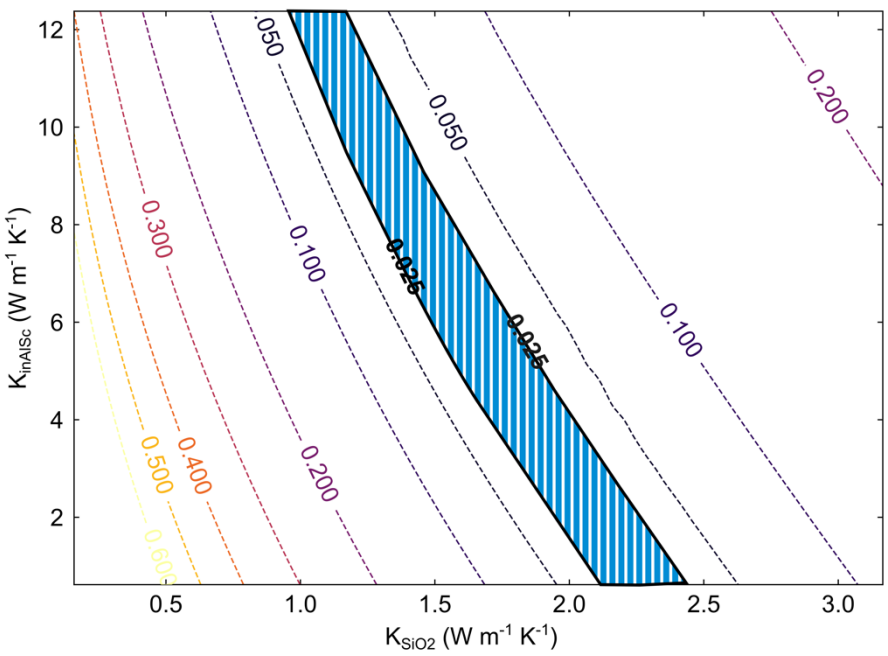

Figure S3. Residual plot for the 150 °C film. The shaded region indicates the .025 residual region.

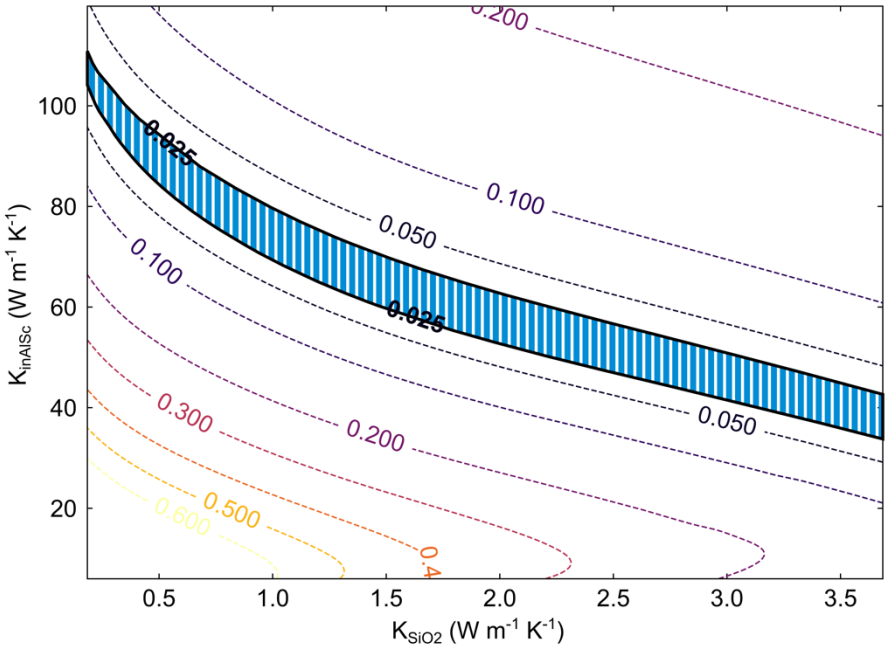

Figure S4. Residual plot for the 25 °C annealed film. The shaded region indicates the .025 residual region.

S2. Electron-phonon coupling measurements.

We further study the scattering mechanisms in aluminum scandium alloys employing an ultrafast (sub-picosecond) pump-probe technique with wavelength tunability into the infrared allowing us to monitor the Drude thermoreflectance response of these alloys. In this technique, a Nd:YVO_4 laser operating at 1 MHz with a central wavelength of ~1040 nm is split with one half being sent into a pump path that is then frequency doubled to 520 nm, and the other being a lower energy probe path. The probe path is sent into an optical parametric amplifier (OPA) which provides wavelength tunability from the visible to near infrared (up to 2500 nm). For our 3000 nm measurements, we use a similar setup utilizing the same Nd:YVO_4 laser operating now at 500 kHz. This setup uses a separate OPA which has wavelength tunability spanning from 2 μm to 16 μm. We measure the pump pulse duration by fitting the thermoreflectance signals of Pt. In this experiment, we pump the electrons in aluminum scandium films out of equilibrium with the phonons using our 520 nm pump laser. Then we probe the thermoreflectance of the heated aluminum scandium as a function of pump-probe delay time for each film where the changes in the dielectric function with temperature are driven by intraband transitions in the aluminum-scandium, and thus dominated by the lattice temperature changes.[13–16] Measurements were taken at 1900 nm for the 25 °C annealed sample and the 450 °C sample. However, for the 150 °C sample measurements were taken at 3000 nm due to the Drude regime being further into the infrared, which we determine based on reflectivity measurements as a function of wavelength for our probe

beam as well as ellipsometry measurements for the 150 °C film. Sample thermoreflectance measurements are shown in Fig. S5. The ellipsometry data was acquired using an M-2000 (M-2000 J.A. Woollam Company) and are shown in Fig. S6.

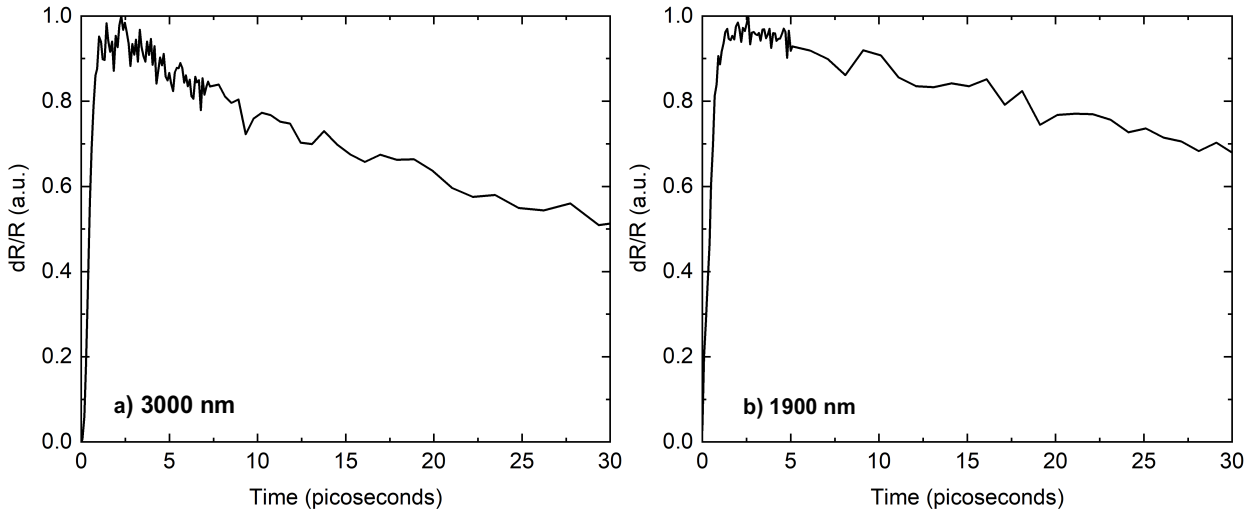

Fig. S5. a) Thermoreflectance measurement of the 25 °C annealed film taken at 3000 nm. **b)** Thermoreflectance measurement 25 °C annealed film taken at 1900 nm. The temporal trends in thermoreflectance on these films are very similar despite the difference in probe wavelength demonstrating the Drude regime for these films.

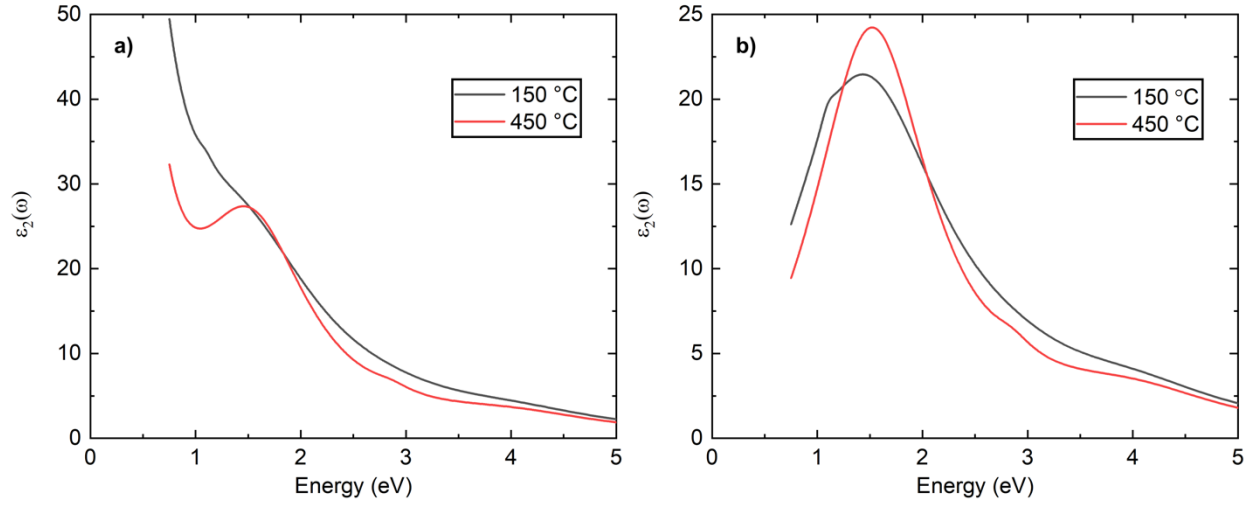

Fig. S6. a) Imaginary part of dielectric function of the 150 °C (black) and 450 °C film (red) obtained from ellipsometry. **b)** Lorentz peaks used in our model.

The ellipsometry data was modeled utilizing Lorentz oscillators to capture the interband transition of our films and a Drude oscillator for the free electron response. We measure increased broadening for the case of the 150 °C film, which has been shown in literature to occur for disordered alloys,[17] and supports the Drude regime being further into the infrared for this film.

S3. Electron-phonon coupling analysis.

We fit our ultrafast pump-probe thermoreflectance data described in Section S2 to the transient lattice temperature profile, as calculated by the two temperature model,[18] given by

$$C_e \frac{\partial T_e}{\partial t} = \nabla (\kappa_e \nabla T_e) - G(T_e - T_l) + S(x,t) \quad \text{(S2)}$$

$$C_l \frac{\partial T_l}{\partial t} = \nabla (\kappa_l \nabla T_l) + G(T_e - T_l)$$

where C_e and C_l are the electronic and lattice heat capacities, respectively, T_e and T_l are the electronic and lattice temperatures, respectively, κ_e and κ_L are the electronic and lattice thermal conductivities, respectively, S is the source term, and G is the electron–phonon coupling factor. The source term is represented by the following equation[19–21]:

$$S(x,t) = (1 - R_{opt}) \frac{1.76J}{2t_p} \cdot sech^2 \left[\left(\frac{1.76(t_o - t)}{t_p} \right) \right] \frac{dI}{dx}. \quad \text{(S3)}$$

In this equation, R_{opt} represents the surface reflectivity, J is the incident fluence, t_p represents the pulse width of the pump pulse, $\frac{dI}{dx}$ is the light intensity profile determined via transfer matrix method[22] with optical constants at the pump wavelength of 520 nm, and t_o is an arbitrary horizontal shift term in case experimental data is off-center from $t = 0$. We measure the input power and the spot-size before each measurement to determine J. We use a two-layer model for our analysis consisting of aluminum scandium and SiO_2, and the constants used in our TTM model can be found in Table S3.

Table S3. Parameters used for two-temperature model analysis. Parameters labeled Fit were determined from TDTR measurements.

Parameters	**AlSc**	**SiO_2**	**AlSc/SiO_2**
Electron heat capacity coefficient γ (J m^{-3} K^{-2})	135 (Ref. 23)	0	-
Electron thermal conductivity κ_e(W m^{-1} k^{-1})	Fit	0	-
Phonon thermal conductivity κ_l (W m^{-1} k^{-1})	3 (Ref. 24)	Fit	-
Phonon heat capacity C_l (MJ $m^{-3}K^{-1}$)	2.3 (Ref. 4)	1.62 (Ref. 5)	-
Refractive index $\hat{n}$(520 nm)	.52+4.98i (Ref. 25)	1.46 (Ref. 26)	-
Electron thermal boundary conductance (MW m^{-2} K^{-1})	-	-	0
Phonon thermal boundary conductance (MW m^{-2} K^{-1})	-	-	Fit

Since our alloys consist of 80% aluminum, we assume refractive index and electronic heat capacity coefficient of aluminum in our analysis. Equations S2 and S3 are solved numerically used the Crank-Nicolson method,[19,27] with a timestep discretization of (dt = 25×10^{-15} s) and space of (dx= 0.5×10^{-9} m) chosen to ensure numerical stability for given material parameters listed in Table S2.

We calculate the lattice and electron temperature from the thermophysical properties listed in Table S2 using TTM simulations. The use of an infrared probe allows us to probe the changes of thermoreflectance of our films in the Drude regime in which the thermoreflectance of our films is

directly proportional to the lattice temperature.[13] Thus we can convert the TTM simulation into the thermoreflectance response by calculating the normalized lattice temperature and comparing it to the normalized reflectivity from our thermoreflectance measurements using this model. Both the model and the experimental data are normalized at the peak thermoreflectivity. We then fit for G using data up to 30 picoseconds of pump-probe time delay. We choose this time range as it provides the early time (few picoseconds) sensitivity to electrons first coupling to phonons in addition to sensitivity to the diffusive process of electrons conducting through the film and then transferring their energy to the phonons through the form of electron-phonon scattering. We plot the early time thermoreflectance response comparing the rise rate of the 150 °C film to the 450 °C film in Fig. S7.

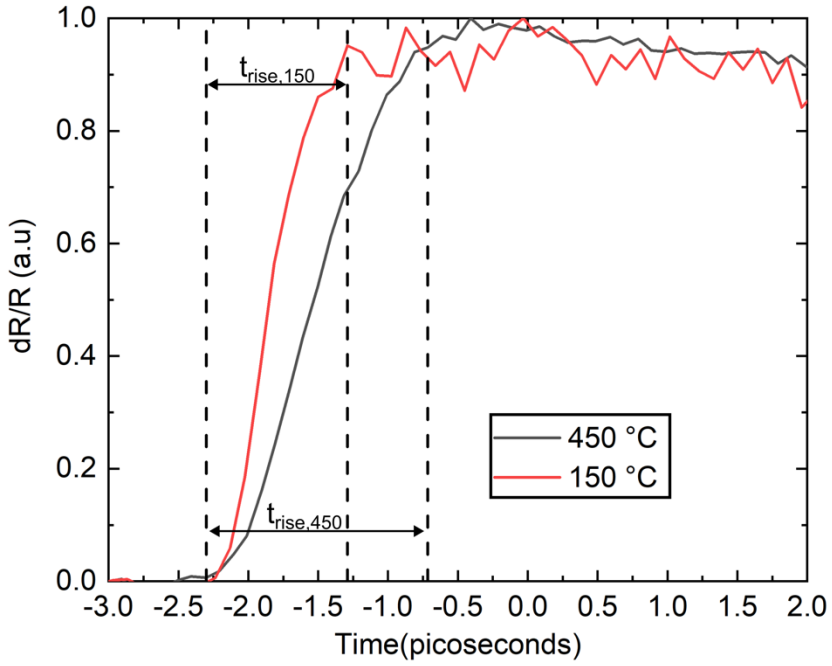

Fig. S7. Thermoreflectance measurement 450 °C sample at 1900 nm in black compared to the thermoreflectance measurement of the 150 °C sample in red. The time it takes for each curve to reach a normalized dR/R of 0.95 is indicated by t_{rise}, and it can be seen that $t_{rise,150}$, the rise time of the 150 °C sample, is shorter than $t_{rise,450}$, the rise time of the 450 °C sample, indicating that the 150 °C film has larger electron-phonon coupling than that of the 450 °C film.

While performing the TTM analysis we verify if the fitting parameters of TTM have sufficient sensitivity in determining *G* accurately. Depending on the quality of the data there exists a range of electron-phonon coupling values for AlSc in our measurements that could be considered as acceptable fits. To determine this uncertainty, we use a type of residual analysis that characterizes the similarity of various fits between the experimental data and our model. We generate the thermoreflectance curve using TTM for a given best-fit set of material properties (Table S2) and then solely perturb *G* and re-fit. How close this modified curve is to the experimental data, in comparison to the best-fit curve, determines the uncertainty bounds on our analysis. To quantify this, we use the following equation from Feser *et al.*[12]:

$$Z(G) \equiv \sqrt{\frac{\sum[dR(t;G_{exact}) - dR(t;G_{perturbed})]^2}{\sum dR(t;G_{exact})^2}}. \quad \text{(S4)}$$

The plot of $Z(G)$ shows the similarity between fits where the curvature on each side of the best-fit value describes how changing the electron-phonon coupling is affecting the uniqueness of fit. A steeper curvature indicates a very tightly bounded best-fit whereas a gradual curvature dictates a best-fit value that is hard to distinguish and has a very large uncertainty in fitting. We choose a 1% residual threshold within which the TTM model generates the same quality of fit to the experimental data as shown in Fig. S8. We include this 1% residual uncertainty to the uncertainty in our *G* calculations. We also notice that the lower and upper bounds of error bar are asymmetric: the curvature is more gradual for higher electron-phonon coupling factors, thus indicating that electron-phonon coupling is affecting the curve less as it increases to higher values.

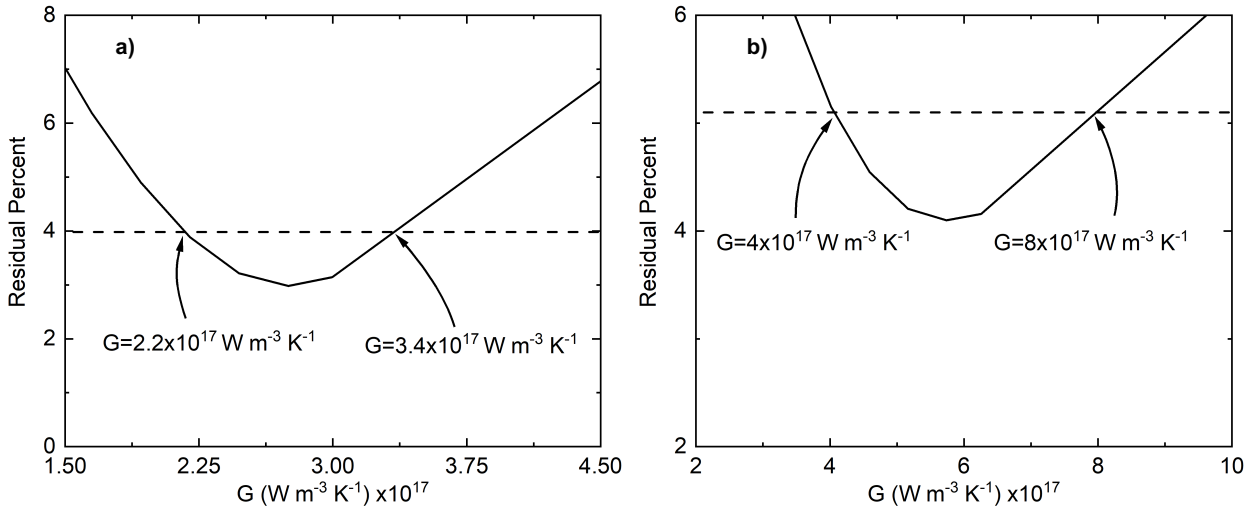

Fig. S8 a) Residual analysis of the 450 °C film. The dashed line indicates the minimum residual (best-fit of G=2.8x10^{17} W m^{-3} K^{-1}) plus 1%. The upper and lower bounds are indicated by the arrows. **b)** Residual analysis of the 150 °C film. The dashed line indicates the minimum residual (best-fit of G=5.7 x10^{17} W m^{-3} K^{-1}) plus one percent.

S4. Electron-phonon coupling sensitivities.

The TTM is suitable to measure the electron-phonon coupling in metals so long as there exists a temperature difference between the electron and phonon channels to drive this coupling. Our TTM predictions show deviations in the electron and lattice temperature that last up to thirty picoseconds, indicating that we have long-time sensitivity to the electron-phonon coupling factor, contrary to a number of prior works using only the first few picoseconds during/after laser heating to measure G.[28–35] As κ_e is much greater than κ_L in our measurements, this results in electron thermal conductivity being the primary mechanism for thermal diffusion. When combined with a sufficiently high electron-phonon coupling factor, temperature differences between the electron and phonon channels last for longer times at the surface of the sample.[36–39] This is due to electrons efficiently diffusing heat away from the surface after laser heating, the phonon system remains at ambient until sufficient energy is lost from the electrons to the lattice. When the electrons begin

to lose energy to the lattice, the phonon system heats up, but the efficient electronic diffusion (i.e., high electronic thermal conductivity) continues to spatially transfer energy away from the probed volume. So conceptually, during every measured time-step when electrons lose energy to phonons, the relatively rapid electronic diffusion creates a local nonequilibrium between the electrons and phonons, leading to a sluggish phonon temperature transient that is out of equilibrium with the electrons due to the low phonon thermal conductivity not being able to diffuse heat out of the surface as rapidly as the electrons. Thus, the ability to probe this lattice temperature response (heating up from the electrons and subsequent slow diffusion away from the surface) allows for resolution of electron-phonon coupling over longer pump-probe delay times than measuring only the hot electron decay over a few picoseconds during/after laser heating.

To quantitatively test this sensitivity concept discussed above, we calculate the sensitivity of our model to the electron-phonon coupling factor. We first perform TTM simulations in the regime where $\kappa_e = 0$ W m^{-1} K^{-1} and G = 1.8x10^{17} W m^{-3} K^{-1}, where the long-time curvature should be dictated by the lattice thermal conductivity and electron-phonon coupling should occur quickly; this plot is shown in Fig. S9a. A similar result should arise if the lattice thermal conductivity is much greater than the electron thermal conductivity which we test by setting $\kappa_l = 2000$ W m^{-1} K^{-1}; this plot is also shown in Fig. S9b. Next, we test the limit where electron-phonon coupling is extremely high by setting G = 1x10^{25} W m^{-3} K^{-1} with all other thermal properties being those of the 25°C annealed film, which results in no difference in electron and phonon temperatures at all times relevant to our pump-probe measurements, as shown in Fig. S9c. When setting G = 1x10^{16} W m^{-3} K^{-1} for the same thermal conductivity values as in Fig. S9c, we see the emergence of a temperature difference between the two channels due to the slow coupling of energy between electrons and phonons (Fig. S9d).

Thus, in these four extreme cases, we see that the sensitivity degree of electron-phonon nonequilibrium during ultrafast laser heating can be defined by the ratio of κ_e/G, as when electron phonon coupling decreases or electron thermal conductivity increases the degree of non-equilibrium increases and thus long-time sensitivity to electron-phonon coupling is increased. This is further emphasized by the temperature response of our aluminum scandium films (Fig. S10) where the 450 °C film, the sample with the highest electronic thermal conductivity, has the longest duration of non-equilibrium. Further, the 150°C film, which we found to have the highest *G* (~6x10^{17} W m^{-3} K^{-1}) and lowest electron thermal conductivity (κ_e = 8.6 W m^{-1} K^{-1}), has the shortest non-equilibrium duration. This is a direct result of faster coupling between the electron and phonon subsystems thus reducing the temperature lag between electrons and phonons. This sensitivity has been described additionally in previous works.[40]

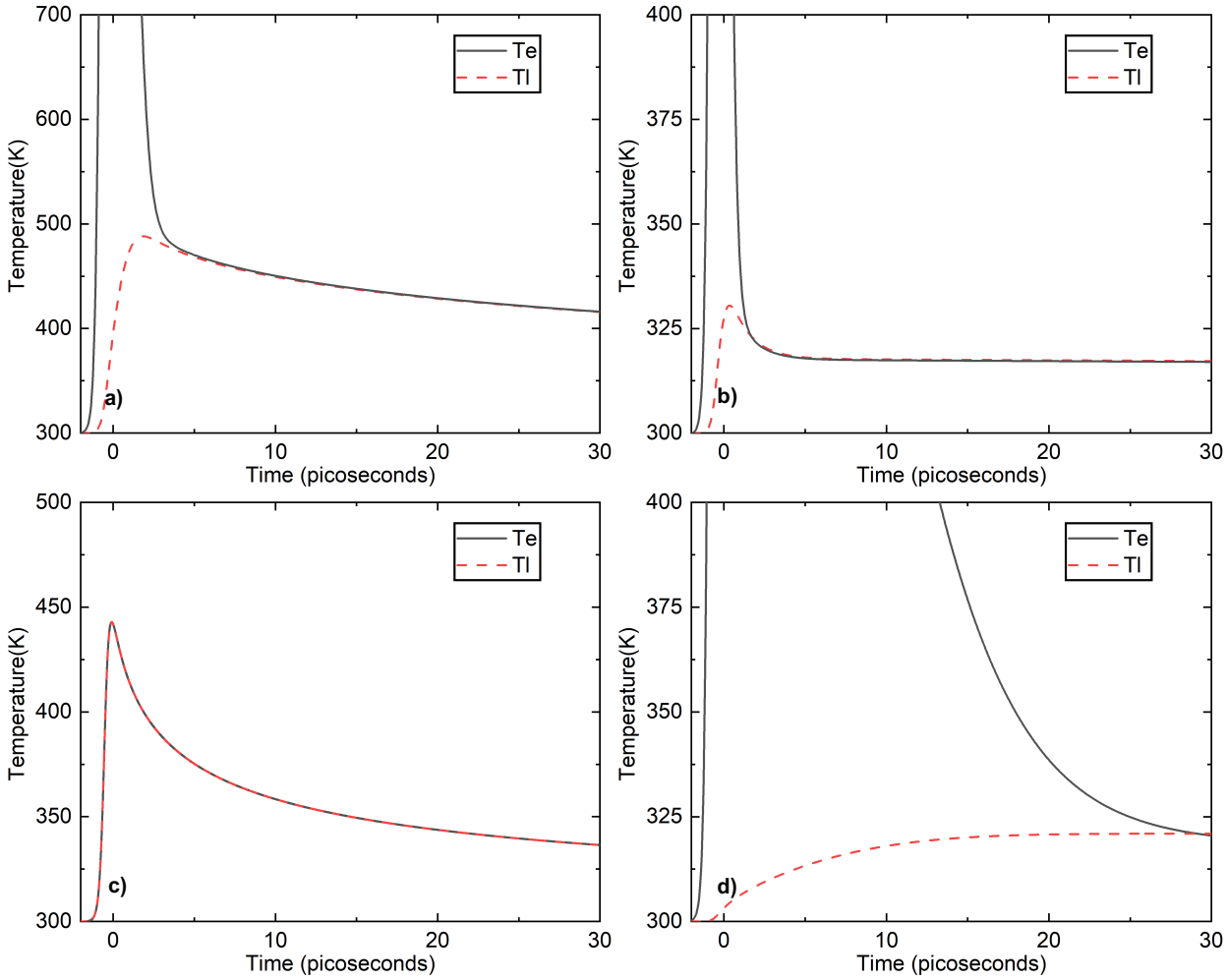

Fig. S9 a) Lattice and electron temperatures plotted against delay time for the case of **a)** κ_e = 0 W m^{-1} K^{-1}, **b)** κ_L = 2000 W m^{-1} K-1, **c)** G=1x10^{25} W m^{-3} K^{-1}, and **d)** G=1x10^{16} W m^{-3} K^{-1} all other thermophysical parameters used are those of the 25°C annealed film**.**

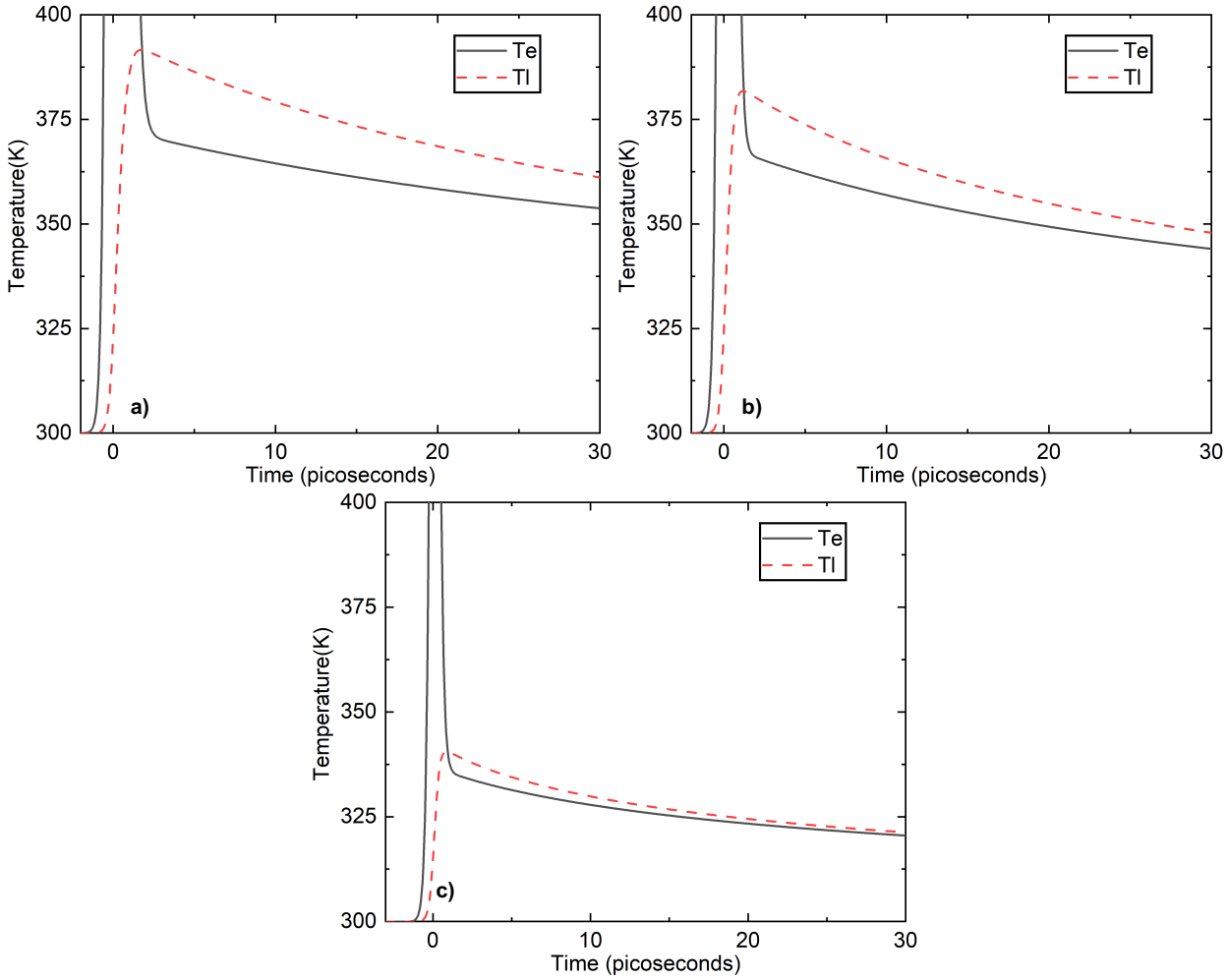

Fig. S10 a) Lattice and electron temperatures plotted against delay time for the case of the **a)** 25 °C annealed sample, κ_e = 67.5 W m^{-1} K^{-1} G=1.8 x 10^{17} W m^{-3} K^{-1}, **b)** 450 °C sample, κ_e = 34.1 W m^{-1} K-1, G=2.8 x 10^{17} W m^{-3} K^{-1}, and **c)** 150 °C sample, κ_e = 8.6 W m^{-1} K^{-1} G=5.7 x 10^{17} W m^{-3} K^{-1}.

S5. Microstructure Characterization

AFM was performed using a Asylum Research Cypher-S instrument in AC mode at tip resonance. A Budget Sensors Tap300Al-G cantilever was used (40 N m^{-1} force constant, 300 kHz resonance frequency). The average grain size was measured by the Hillard ASTM E112 single circle

procedure, 13 total were done with 3 randomly sized and placed circles to obtain average grain size as well as the standard deviation. Sample AFM images are shown in Fig. S11.

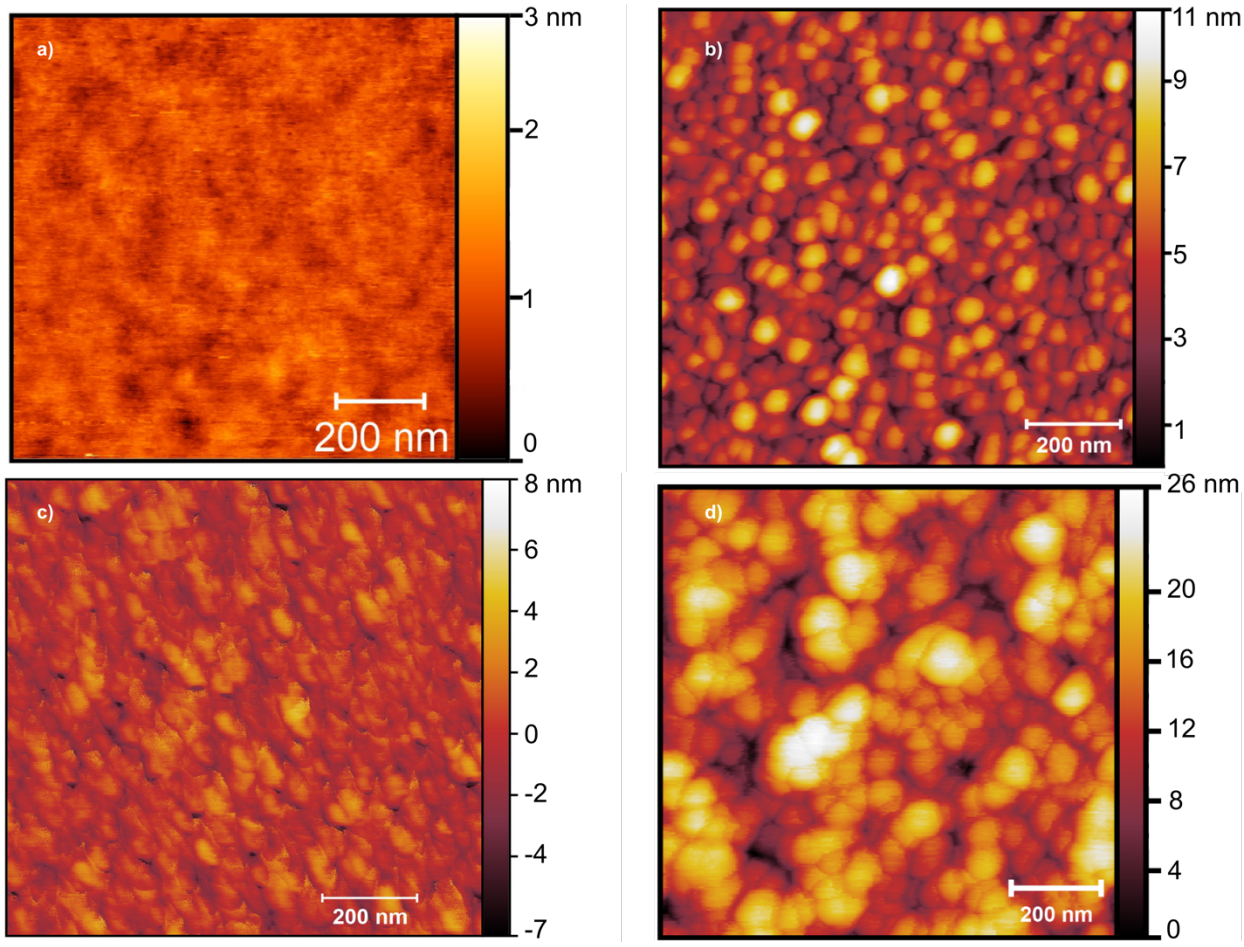

Fig. S11 AFM images for the 25°C un-annealed sample **a)** the 150°C film **b)** the 300°C film **c)** and the 450°C sample **d)**. The grain sizes were found to be 48 ± 1 nm, 50 ± 3 nm, and 65 ± 1 nm for the 150°C, 300°C, and 450°C films respectively. The grain size for the 25°C un-annealed sample was not able to be determined.

In addition to the AFM images we show high-angle annular dark-field scanning transmission electron microscopy (HAADF STEM) images adapted from Esteves *et al.*[41] for the 150 °C film Fig. S12 and the 450 °C film Fig. S13 indicating increased crystallinity for the 450 °C film.

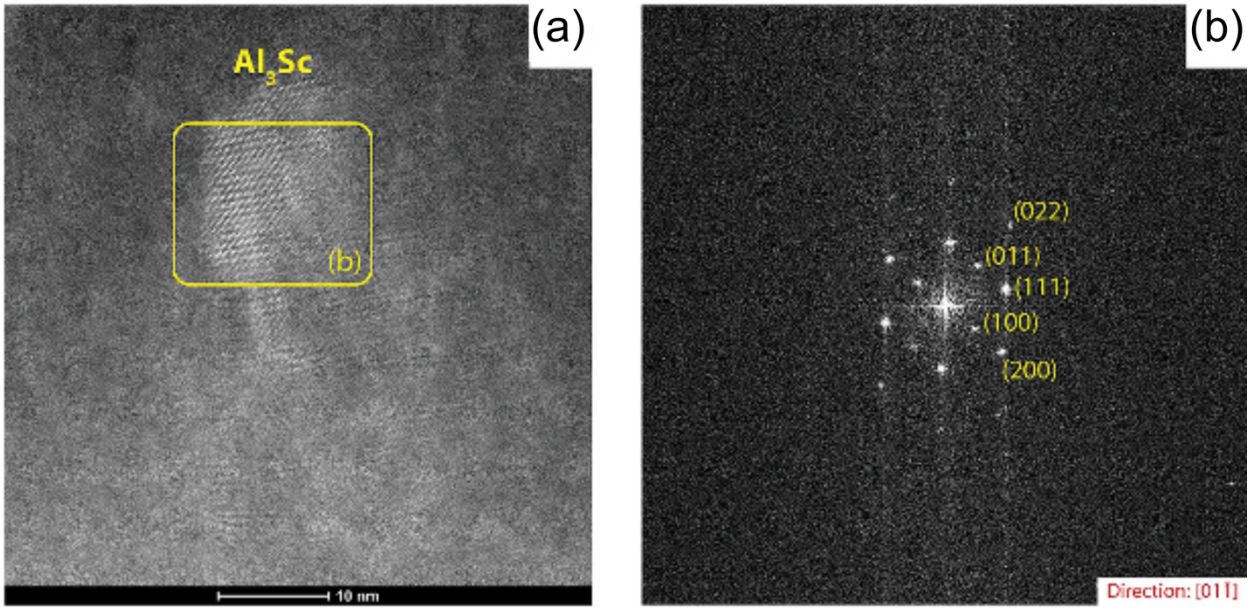

Fig. S12 HAADF STEM image for the 150 °C film a) and the Fourier transform of the indicated region b) which shows the 100 reflection that is unique to the space group of Al_3Sc. Reprinted from Vacuum, 200, G. Esteves, Formation of Al3Sc in Al0.8Sc0.2 thin films, Page 7, 2022, with permission from Elsevier.

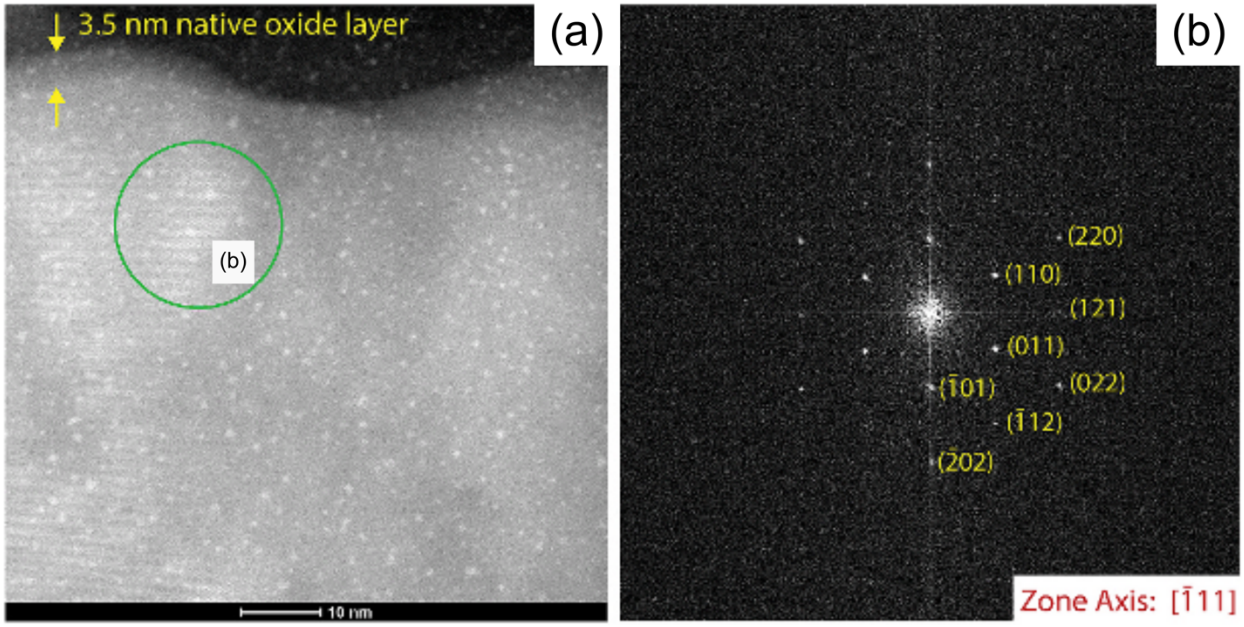

Fig. S13 HAADF STEM image for the 450 °C film a) and the Fourier transform of the indicated region b). The 011 and 121 reflections are unique to Al_3Sc. Reprinted from Vacuum, 200, G. Esteves, Formation of Al3Sc in Al0.8Sc0.2 thin films, Page 7, 2022, with permission from Elsevier.

S6. Thermal Conductivity Analysis & Estimation

For our thermal conductivity measurements, we measured the largest deviation between the values calculated via the WFL and the mean value from our TDTR measurements for the case of the 450 °C film. We attribute the deviation in thermal conductivity and WFL derived thermal conductivity to a possible Lorenz number deviation for our films. For our WFL calculated thermal conductivities we used the room temperature Sommerfeld value of the Lorenz number $L_0 = 2.45 \times 10^{8}$ W Ω K^{-2}. It is possible that the chosen Lorenz number is not accurate for the samples with greater formation of Al_3Sc as opposed to the solid solutions. In fact, it has been shown in multiple metallic alloys that the Lorenz number could be up to 30% smaller than L_0.[42–44] This deviation was attributed to additional inelastic electron-phonon scattering processes that could be occurring at the surface of the film or at grain boundaries. As the grain sizes for our film are also on the order of the film thicknesses, such as in the aforementioned studies which monitor deviations in L_0, we posit that we could be seeing a similar reduction in L_0 due to inelastic electron-phonon scattering processes. For illustration we assume a slightly smaller reduction to L_0 of 20% and plot our Figure 2 with the adjusted WFL thermal conductivities as Fig. S14.

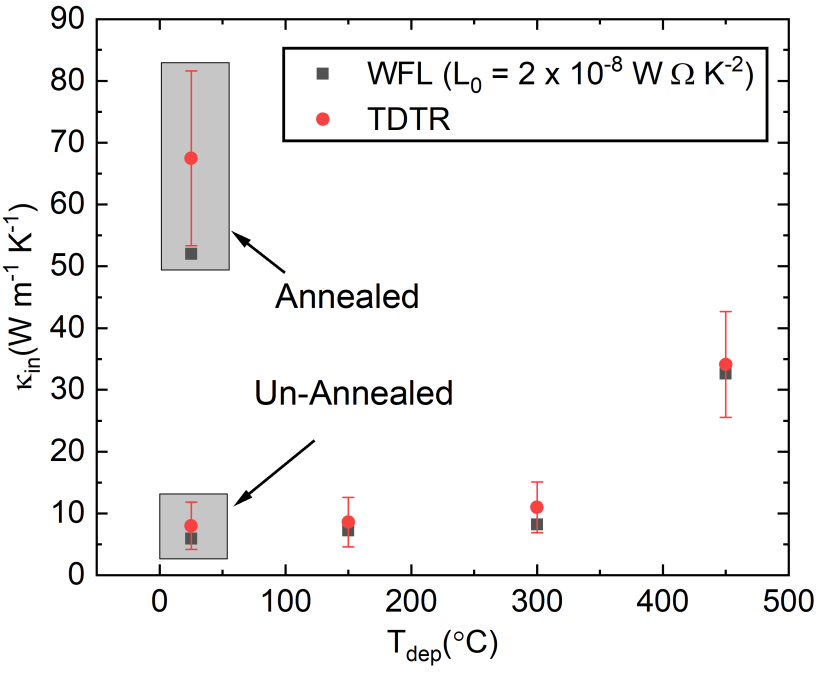

Fig. S14 In-plane thermal conductivity plotted against deposition temperature comparing TDTR data (red) against WFL calculated data assuming a Lorenz number of L_0 = 2 x 10^8 W Ω K^{-2}.

In addition, we quantify the electron-phonon coupling contribution to our thermal conductivity trends by performing a rough calculation based on kinetic theory. First, to estimate the contribution of electron-phonon coupling to the thermal conductivity, we utilize the following equation to calculate the electron-phonon scattering rate under the assumption that $T_E >> T_L$[13,23]:

$$G = \frac{m_e \pi^2 n_e C_s^2}{6 \tau_{e-p} T_e}$$

Where m_e, n_e ,τ_{e-p}, C_s, and G are the effective mass, electron density, electron-phonon scattering rate, speed of sound and electron-phonon coupling factor respectively. We assume the effective mass of Al_3Sc as being the rest mass of an electron and for the electron-phonon coupling factor

we use our results from the TTM analysis. We calculate the electron density as 5.5 x 10^{28} m^{-3} using the fermi velocity for Al_3Sc determined from Adelmann *et al.*[45] For the speed of sound, C_s , we use a value of 5266 m s^{-1} calculated from averaging the longitudinal and transverse speed of sound of Al_3Sc[46]:

$$C_s = [\frac{1}{3}(\frac{1}{V_L} + \frac{2}{V_T})]^{-\frac{1}{3}}$$

Where V_L, and V_T are the longitudinal and transverse speed of sound respectively. According to the kinetic theory, $\kappa_e = \frac{1}{3} C_e v_f^2 \tau_e$, where C_e is the electronic heat capacity, v_f is the fermi velocity, and τ_e represents the total electronic scattering rate. Thus, by determining the total electron scattering rate, fermi velocity, and electronic heat capacity we can obtain an estimate for the electronic thermal conductivity. We use the fermi velocity as that of Al_3Sc and the electronic heat capacity as that of Al.[23,45]

In addition to electron-phonon scattering, we also consider the contribution of electron-electron scattering to the total electron scattering. We calculate the electron-electron scattering time, τ_{e-e}, from the fermi-liquid theory[47,48] using the properties of aluminum, which we find to be 3 femtoseconds. Then, to calculate the total electronic scattering time, we then apply Matthiessen's rule:

$$\frac{1}{\tau_e} = \frac{1}{\tau_{e-p}} + \frac{1}{\tau_{e-e}}$$

Electron phonon coupling is plotted against our calculated values and the experimental values for comparison in Fig. S15. Here we see that our calculation is closer to the experimental thermal

conductivity results for the higher deposition temperature samples. We believe this results from the model failing to account for other scattering mechanisms such as defect scattering, which would occur more frequently in the more heavily disordered lower deposition temperature samples, ultimately resulting in our calculation over-predicting their thermal conductivity.

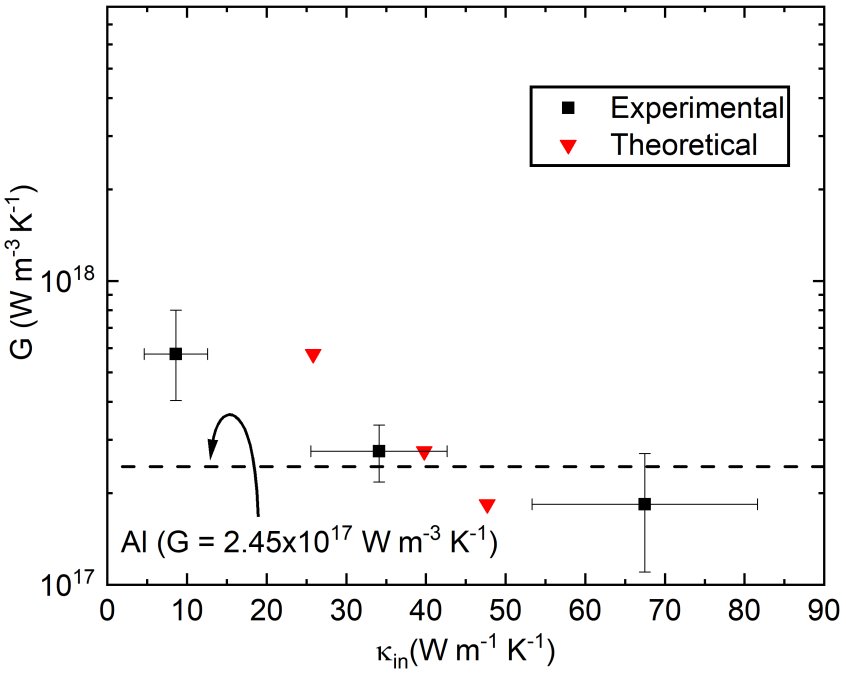

Fig. S15 Electron-phonon coupling plotted against in-plane thermal conductivity comparing our results (black) and our calculated values (red).

References

[1] D.G. Cahill, "Analysis of heat flow in layered structures for time-domain thermoreflectance," Review of Scientific Instruments **75**(12), 5119–5122 (2004).
[2] D.G. Cahill, K. Goodson, and A. Majumdar, "Thermometry and Thermal Transport in Micro/Nanoscale Solid-State Devices and Structures," J Heat Transfer **124**(2), 223–241 (2002).
[3] Z. Hashin, and S. Shtrikman, "Conductivity of Polycrystals," Physical Review **130**(1), 129 (1963).
[4] W.J. Parker, R.J. Jenkins, C.P. Butler, and G.L. Abbott, "Flash Method of Determining Thermal Diffusivity, Heat Capacity, and Thermal Conductivity," J Appl Phys **32**(9), 1679–1684 (1961).
[5] J.L. Braun, C.H. Baker, A. Giri, M. Elahi, K. Artyushkova, T.E. Beechem, P.M. Norris, Z.C. Leseman, J.T. Gaskins, and P.E. Hopkins, "Size effects on the thermal conductivity of amorphous silicon thin films," RAPID COMMUNICATIONS PHYSICAL REVIEW B **93**, 140201 (2016).
[6] M.S. Bin Hoque, Y.R. Koh, K. Aryana, E.R. Hoglund, J.L. Braun, D.H. Olson, J.T. Gaskins, H. Ahmad, M.M.M. Elahi, J.K. Hite, Z.C. Leseman, W.A. Doolittle, and P.E. Hopkins, "Thermal conductivity measurements of sub-surface buried substrates by steady-state thermoreflectance," Review of Scientific Instruments **92**(6), (2021).
[7] C. Cancellieri, E.A. Scott, J. Braun, S.W. King, R. Oviedo, C. Jezewski, J. Richards, F. La Mattina, L.P.H. Jeurgens, and P.E. Hopkins, "Interface and layer periodicity effects on the thermal conductivity of copper-based nanomultilayers with tungsten, tantalum, and tantalum nitride diffusion barriers," J Appl Phys **128**(19), 195302 (2020).
[8] P. Jiang, B. Huang, and Y.K. Koh, "Accurate measurements of cross-plane thermal conductivity of thin films by dual-frequency time-domain thermoreflectance (TDTR)," Review of Scientific Instruments **87**(7), 75101 (2016).
[9] Y.K. Koh, S.L. Singer, W. Kim, J.M.O. Zide, H. Lu, D.G. Cahill, A. Majumdar, and A.C. Gossard, "Comparison of the 3ω method and time-domain thermoreflectance for measurements of the cross-plane thermal conductivity of epitaxial semiconductors," J Appl Phys **105**(5), 54303 (2009).
[10] M.S. Bin Hoque, Y.R. Koh, J.L. Braun, A. Mamun, Z. Liu, K. Huynh, M.E. Liao, K. Hussain, Z. Cheng, E.R. Hoglund, D.H. Olson, J.A. Tomko, K. Aryana, R. Galib, J.T. Gaskins, M.M.M. Elahi, Z.C. Leseman, J.M. Howe, T. Luo, S. Graham, M.S. Goorsky, A. Khan, and P.E. Hopkins, "High In-Plane Thermal Conductivity of Aluminum Nitride Thin Films," ACS Nano **15**(6), 9588–9599 (2021).
[11] Z. Cheng, Y.R. Koh, A. Mamun, J. Shi, T. Bai, K. Huynh, L. Yates, Z. Liu, R. Li, E. Lee, M.E. Liao, Y. Wang, H.M. Yu, M. Kushimoto, T. Luo, M.S. Goorsky, P.E. Hopkins, H. Amano, A. Khan, and S. Graham, "Experimental observation of high intrinsic thermal conductivity of AlN," Phys Rev Mater **4**(4), 044602 (2020).
[12] J.P. Feser, and D.G. Cahill, "Probing anisotropic heat transport using time-domain thermoreflectance with offset laser spots □," Rev. Sci. Instrum **83**, 104901 (2012).
[13] J.A. Tomko, S. Kumar, R. Sundararaman, and P.E. Hopkins, "Temperature dependent electron-phonon coupling of Au resolved via lattice dynamics measured with sub-picosecond infrared pulses," J Appl Phys **129**(19), 193104 (2021).
[14] M. Kaveh, and N. Wiser, "Electron-electron scattering in conducting materials," Adv Phys **33**(4), 257–372 (1984).
[15] R.W. Schoenlein, W.Z. Lin, J.G. Fujimoto, and G.L. Eesley, "Femtosecond studies of nonequilibrium electronic processes in metals," Phys Rev Lett **58**(16), 1680–1683 (1987).

[16] T. Heilpern, M. Manjare, A.O. Govorov, G.P. Wiederrecht, S.K. Gray, and H. Harutyunyan, "Determination of hot carrier energy distributions from inversion of ultrafast pump-probe reflectivity measurements," Nat Commun **9**(1), (2018).
[17] J. Rivory, "Comparative study of the electronic structure of noble-metal-noble-metal alloys by optical spectroscopy," Phys Rev B **15**(6), 3119 (1977).
[18] S.I. Anisimov, B.L. Kapeliovich, T.L. Perel'Man, S.I. Anisimov, B.L. Kapeliovich, and T.L. Perel'Man, "Electron emission from metal surfaces exposed to ultrashort laser pulses," JETP **39**, 375–377 (1974).
[19] D.H. Olson, M.G. Sales, J.A. Tomko, T.F. Lu, O. V. Prezhdo, S.J. McDonnell, and P.E. Hopkins, "Band alignment and defects influence the electron-phonon heat transport mechanisms across metal interfaces," Appl Phys Lett **118**(16), 163503 (2021).
[20] J.K. Chen, J.E. Beraun, and C.L. Tham, "Investigation of thermal response caused by pulse laser heating," Numeri Heat Transf A Appl **44**(7), 705–722 (2003).
[21] J. Sotrop, A. Kersch, M. Domke, G. Heise, and H.P. Huber, "Numerical simulation of ultrafast expansion as the driving mechanism for confined laser ablation with ultra-short laser pulses," Appl Phys A Mater Sci Process **113**(2), 397–411 (2013).
[22] M. Born, and E. Wolf, "Principles of Optics 7th edition," Principles of Optics Electromagnetic Theory of Propagation Interference and Diffraction of Light, 1–952 (1999).
[23] Z. Lin, L. V. Zhigilei, and V. Celli, "Electron-phonon coupling and electron heat capacity of metals under conditions of strong electron-phonon nonequilibrium," Phys Rev B Condens Matter Mater Phys **77**(7), (2008).
[24] A. Jain, and A.J.H. McGaughey, "Thermal transport by phonons and electrons in aluminum, silver, and gold from first principles," Phys Rev B **93**(8), 081206 (2016).
[25] F. Cheng, P.H. Su, J. Choi, S. Gwo, X. Li, and C.K. Shih, "Epitaxial Growth of Atomically Smooth Aluminum on Silicon and Its Intrinsic Optical Properties," ACS Nano **10**(11), 9852–9860 (2016).
[26] I.H. Malitson, "Interspecimen Comparison of the Refractive Index of Fused Silica*,†," JOSA, Vol. 55, Issue 10, Pp. 1205-1209 **55**(10), 1205–1209 (1965).
[27] B. Raton, A. Arbor, and L. Tokyo, "Finite Difference Methods in Heat Transfer," Finite Difference Methods in Heat Transfer, (2017).
[28] S.D. Brorson, A. Kazeroonian, J.S. Moodera, D.W. Face, T.K. Cheng, E.P. Ippen, M.S. Dresselhaus, and G. Dresselhaus, "Femtosecond room-temperature measurement of the electron-phonon coupling constant γ in metallic superconductors," Phys Rev Lett **64**(18), 2172 (1990).
[29] A. Giri, J.T. Gaskins, B.M. Foley, R. Cheaito, and P.E. Hopkins, "Experimental evidence of excited electron number density and temperature effects on electron-phonon coupling in gold films," J Appl Phys **117**(4), 44305 (2015).
[30] P.E. Hopkins, J.L. Kassebaum, and P.M. Norris, "Effects of electron scattering at metal-nonmetal interfaces on electron-phonon equilibration in gold films," J Appl Phys **105**(2), 23710 (2009).
[31] R.H.M. Groeneveld, R. Sprik, and A. Lagendijk, "Femtosecond spectroscopy of electron-electron and electron-phonon energy relaxation in Ag and Au," Phys Rev B **51**(17), 11433 (1995).
[32] R.H.M. Groeneveld, R. Sprik, and A. Lagendijk, "Effect of a nonthermal electron distribution on the electron-phonon energy relaxation process in noble metals," Phys Rev B **45**(9), 5079 (1992).
[33] C.K. Sun, F. Vallée, L.H. Acioli, E.P. Ippen, and J.G. Fujimoto, "Femtosecond-tunable measurement of electron thermalization in gold," Phys Rev B **50**(20), 15337 (1994).

[34] C.K. Sun, F. Vallée, L. Acioli, E.P. Ippen, and J.G. Fujimoto, "Femtosecond investigation of electron thermalization in gold," Phys Rev B **48**(16), 12365 (1993).
[35] J. Hohlfeld, S.S. Wellershoff, J. Güdde, U. Conrad, V. Jähnke, and E. Matthias, "Electron and lattice dynamics following optical excitation of metals," Chem Phys **251**(1–3), 237–258 (2000).
[36] A. Giri, J.T. Gaskins, B.F. Donovan, C. Szwejkowski, R.J. Warzoha, M.A. Rodriguez, J. Ihlefeld, and P.E. Hopkins, "Mechanisms of nonequilibrium electron-phonon coupling and thermal conductance at interfaces," J Appl Phys **117**(10), (2015).
[37] P. Karna, M.S. Bin Hoque, S. Thakur, P.E. Hopkins, and A. Giri, "Direct Measurement of Ballistic and Diffusive Electron Transport in Gold," Nano Lett **23**(2), 491–496 (2023).
[38] G.-M. Choi, R.B. Wilson, and D.G. Cahill, "Indirect heating of Pt by short-pulse laser irradiation of Au in a nanoscale Pt/Au bilayer," Phys Rev B **89**, 64307 (2014).
[39] W. Wang, and D.G. Cahill, "Limits to Thermal Transport in Nanoscale Metal Bilayers due to Weak Electron-Phonon Coupling in Au and Cu," Phys. Rev. Lett **109**, 175503 (2012).
[40] Z. Lu, A. Vallabhaneni, B. Cao, and X. Ruan, "Phonon branch-resolved electron-phonon coupling and the multitemperature model," Phys Rev B **98**(13), (2018).
[41] G. Esteves, J. Bischoff, E.W.S. Schmidt, M.A. Rodriguez, S.G. Rosenberg, and P.G. Kotula, "Formation of Al3Sc in Al0.8Sc0.2 thin films," Vacuum **200**, (2022).
[42] X. Zheng, D.G. Cahill, P. Krasnochtchekov, R.S. Averback, and J.C. Zhao, "High-throughput thermal conductivity measurements of nickel solid solutions and the applicability of the Wiedemann–Franz law," Acta Mater **55**(15), 5177–5185 (2007).
[43] L. Piraux, M. Cassart, J.S. Jiang, J.Q. Xiao, and C.L. Chien, "Magnetothermal transport properties of granular Co-Ag solids," Phys Rev B **48**(1), 638 (1993).
[44] A.D. Avery, S.J. Mason, D. Bassett, D. Wesenberg, and B.L. Zink, "Thermal and electrical conductivity of approximately 100-nm permalloy, Ni, Co, Al, and Cu films and examination of the Wiedemann-Franz Law," Phys Rev B Condens Matter Mater Phys **92**(21), 214410 (2015).
[45] J.P. Soulié, K. Sankaran, V. Founta, K. Opsomer, C. Detavernier, J. Van de Vondel, G. Pourtois, Z. Tőkei, J. Swerts, and C. Adelmann, "Al3Sc thin films for advanced interconnect applications," Microelectron Eng **286**, 112141 (2024).
[46] D. Chen, Z. Chen, Y. Wu, M. Wang, N. Ma, and H. Wang, "First-principles investigation of mechanical, electronic and optical properties of Al3Sc intermetallic compound under pressure," Comput Mater Sci **91**, 165–172 (2014).
[47] V.A. Gasparov, and R. Huguenin, "Electron-phonon, electron-electron and electron-surface scattering in metals from ballistic effects," Adv Phys **42**(4), 393–521 (1993).
[48] D. Pines, and P. Nozières, "The theory of quantum liquids normal fermi liquids," The Theory of Quantum Liquids Normal Fermi Liquids **1**, 1–355 (2018).